Progress in Natural Science: Materials International 36 (2026) 65–75

HOSTED BY

Contents lists available at ScienceDirect

Progress in Natural Science: Materials International

journal homepage: www.elsevier.com/locate/pnsmi

Non-Hermitian phonon quantization controlled through different phases of Eu^{3+}: $BiPO_4$

Muhammad Qasim Khan[a,1], Iqbal Hussain[a,1], Faisal Nadeem[a,1], Nadir Khan[a], Mudassir[a], Huanrong Fan[a,b,*], Changbiao Li[a,**], Yanpeng Zhang[a,***]

[a] Key Laboratory for Physical Electronics and Devices of the Ministry of Education & Shaanxi Key Lab of Information Photonic Technique, Xi'an Jiaotong University, Xi'an, 710049, China
[b] College of Electrical and Information Engineering, Hunan University of Technology, Zhuzhou, 412007, China

ARTICLE INFO

Keywords:
Destructive/constructive quantization
Phonon quantization
Different phases
Temporal autler townes splitting

ABSTRACT

This study investigates a novel phenomenon of non-Hermitian phonon quantization in Eu^{3+}: $BiPO_4$ crystals controlled by different phases. The hexagonal (H) -phase (0.5:1) with low symmetry has strongest destructive gamma phonon quantization as compare to high symmetry phases H-Monoclinic (M) phases (12:1, 1:1) in fluorescence (FL) region, while strong constructive dominant dressing quantization exhibits due to higher phonon density of states in spontaneous four wave mixing (SFWM) region. Strong Spectral Autler-Townes (SAT) is observed in (6:1) phase at small angle and time gate position (GP = 500 ns), while, strong Temporal Autler-Townes (TAT) is studied at GP = 1ns. Also, (6:1) exhibits angle destructive quantization in FL region. Comparison between the H-M (12:1) phase and H = M (6:1) phases reveals that the H-M phase exhibits stronger destructive gamma quantization in FL region due to larger gamma phonon in (12:1) phase. Moreover, H-phase (0.5:1) exhibits large number of phonon density and shows strong constructive quantization as compare to M-phase (7:1) in SWFM region. Additionally, two destructive dressing quantization are observed in fluorescence region where gamma quantization is affected by additional laser. This work establishes a deterministic relation between non-Hermitian phonon quantization and different phases of Eu^{3+}: $BiPO_4$, enabling applications in quantum memory and tunable bandpass filters. The Band pass filter control through phonon quantization with different phases of Eu^{3+}: $BiPO_4$.

1. Introduction

Rare-earth ion-doped crystals are valuable options for quantum storage because of their important roles in light and photonic technologies [1–3]. Among these, Eu^{3+}-doped crystals are important due to their long coherence times and effective atomic state transitions that allow for accurate regulation via nonlinear optical processes like photonic entanglement generation in the crystal lattice and electromagnetically induced transparency (EIT) [4]. EIT is an important quantum optical phenomenon that is observed in a variety of quantum systems and permits the controlling of light-matter interactions, which are significantly impacted by dressing field splitting effects [5–7]. Because of their excellent ability to maintain coherence, Eu^{3+}-doped crystals are especially suitable for advanced quantum uses like integrated photonic devices, quantum memory, and all-optical switching [8].

Europium (Eu^{3+}) is interesting dopant in solid-state materials, because of its strong lattice-spin coupling, high sensitivity and non-degenerate multiplet structures [9,10]. For lanthanide doping, Bismuth phosphate ($BiPO_4$) is one of the most researched host materials [11]. By improving optical performance, the similar ionic radii of Eu^{3+} (1.07 Å) and Bi^{3+} (1.11A) enable effective dopant dressing [12]. Additionally, $BiPO_4$ has different phonon dressing that are controlled by their site symmetries (C_1, C_2 and C_1+ C_2) lead to different crystal-field (CF) splitting in the Eu^{3+} ion ($^5D_0 \rightarrow {}^7F_1$ transition) [13].

These variations affect their electron-phonon coupling and optical properties. Notably, phonon detuning effects have a major effect on

* Corresponding author. College of Electrical and Information Engineering, Hunan University of Technology, Zhuzhou, 412007, China.
** Corresponding author.
*** Corresponding author.
E-mail addresses: fanhuanrong001@stu.xjtu.edu.cn (H. Fan), cbli@mail.xjtu.edu.cn (C. Li), ypzhang@mail.xjtu.edu.cn (Y. Zhang).
[1] These authors contributed equally to this work.

https://doi.org/10.1016/j.pnsc.2025.09.007
Received 28 June 2025; Received in revised form 11 September 2025; Accepted 25 September 2025
Available online 18 December 2025

phase transitions in lanthanide-doped $BiPO_4$ and play a key role in adjusting the optical and structural behavior of the material [14–17]. Furthermore, the optical dressing and crystal phase transitions utilized to alter the atomic coherence time [18]. A predictable relationship between thermal-phonon dressings and non-Hermitian interference effects is being observed in rare-earth-doped microcrystals [19], emphasizing the important role that phonon interactions play in determining quantum optical responses.

Our atomic-like system enables direct control of the dressing to diphase rate ratio, contrasting with traditional waveguide and cavity systems that manipulate coupling and gain-loss [20,21]. While previous non-Hermitian interaction [7,22] relied on strong and weak coupling, our system achieves natural non-Hermitian interactions through quantized constructive and destructive interference. This represents the first demonstration of exceptional point tuning via intrinsic quantization effects, bypassing artificial gain-loss modulation [23].

Lattice symmetry play a significant role in the determination of physical properties these crystals [5,6]. The quantization effect and size limitation impact the symmetry breakdown in materials. The bulk 3D materials with high symmetry (zero-dimensional quantization), the bandgaps are dominant, while in 0D quantum dots have low symmetry, energy levels overcome due to three-dimensional quantization. In 1D and 2D materials, bandgaps and energy levels both coexist [24]. Reducing material size can cause symmetry breakdown, as demonstrated in lanthanide-doped nanoprobes. Additionally, quantization effects, such as crystal field (CF) quantization driven by internal Stark fields, can achieve symmetry breakdown in atomic-like system. This has been observed in ion-doped microcrystals under non-resonant excitation [25,26]. Photon-phonon dressing, arising from quantization, has been studied in multi-wave mixing within five-level atomic systems [27], while phonon dressing controlled atomic coherence time during phase transitions [8].

Phonon quantization plays a key role in rare-earth-doped materials, where lattice vibrations (phonon) and crystal symmetry strongly influence optical properties. Studies in Eu^{3+}-doped $BiPO_4$ reveal how phase transitions modify phonon dressing effects [15,27], while work on Eu_2ZnIrO_6 demonstrates direct coupling between phonons and electronic excitations [9]. These findings support our investigation of phonon-mediated spectral control. This based on previous study of symmetry-dependent phonon interactions [10,16] while new direction for quantum control through phonon quantization in rare-earth crystals.

Phase transitions is critical in determining the physical properties of functional crystals like $BiPO_4$ [5,6,10–28]. Comprehensive studies have revealed the structural, electronic, and optical characteristics of its various phases [12,16,29], particularly in Eu^{3+}-doped systems where composition dictates phase formation [15]. The transformation from monoclinic (LTMP/HTMP) to hexagonal (HP) phases is achieved through Ln^{3+}/Eu^{3+} doping, with specific ratios producing distinct phase mixtures: 6:1 (balanced HP/LTMP), 1:1 (HP-dominant), 0.5:1 (pure HP), 7:1 (pure LTMP), and 12:1 (HP-dominant) [30]. Each combination exhibits unique phonon detuning due to phase-dependent lattice vibrations, demonstrating how structural changes directly modify phonon dressing and dynamics.

Recent advancements in non-Hermitian photonics have been largely driven by engineered systems such as meta-surfaces and plasmonic waveguides [31,32] where exceptional points and Fano resonances are controlled through geometric design and external gain-loss modulation. Similarly, the broader potential of lanthanide-doped materials is well-established [33] Our work bridges these concepts by demonstrating that complex non-Hermitian phenomena including destructive/constructive quantization and Autler-Townes splitting can be achieved intrinsically in a bulk rare-earth-doped crystal without artificial nano-structuring. By leveraging the host's crystallographic phase transition, we provide a deterministic materials-based knob to control phonon dressing and access exceptional points, offering a complementary approach to the external control methods employed in plasmonic systems [34]. This intrinsic control mechanism is particularly advantageous for developing robust and tunable quantum memory elements and optical filters within a single material platform.

In this paper, we investigated non-Hermitian phonon quantization controlled by phase transitions between monoclinic (LTMP) and hexagonal (HP) phases in Eu^{3+}: $BiPO_4$ crystals. By varying different parameters (time gate position (GP), time gate width (GW), power, quantization angle, phase transition and bandwidth (BW)), the phonon quantization is studied. We demonstrate that in FL region, the low-symmetry H-phase (0.5:1) shows the strongest destructive gamma phonon quantization, while in SFWM region shows dominant constructive quantization because of the greater phonon density of states. This study has the advantage of demonstrating phonon-mediated quantum control without the need for artificial gain-loss engineering. This offers applications in hyperfine structure manipulation for quantum technologies and adjustable bandpass filters.

2. Experimental setup and quantization

2.1. Experimental setup

Gamma phonon quantization and phonon density of state are studied in pure hexagonal phase, pure monoclinic phase and mixed (hexagonal + monoclinic) phase in Eu^{3+}: $BiPO_4$ with C2, C1 and C2+C1 symmetry, respectively. The Eu^{3+}: $BiPO_4$ have different molar ratios in these experiments by utilizing the different combination and concentrations of hexagonal phase (HP) and monoclinic (MP) phase with a fixed concentration of 5 % in each sample. The sample (7:1) corresponds to the pure M-phase, (6:1) corresponds to the mixed [half H (50 %) + half M (50 %)] phase, (1:1) corresponds to the mixed [more H (75 %) + less M (25 %)] phase, (12:1) corresponds to the mixed [more H (51 %) + less M (49 %)] phase, and (0.5:1) corresponds to the pure H phase. In our experiment, the samples were held in a cryostat (CFM-102) with liquid nitrogen as temperature controller.

We used two tuneable dye laser (narrow band 2 GHz) and (broadband 5 GHz) driven by an injection-locked single-mode Nd: YAG laser (Continuum Power lite DLS 9010, 10Hz repetition rate, 5ns pulse width) to produce a pumping field. Fig. 1(a1) shows pure Eu^{3+} ion $^5D_0$ (excited states) to 7F1 (ground states) transition without CF splitting level. Fig. 1 (a2) shows $^5D_0$ to $^7F_1$ transition of Eu^{3+}: $BiPO_4$ with pure crystal field splitting at ground state. Fig. 1(b1-b3) shows the fine structure of Eu^{3+}: $BiPO_4$ crystals for three CF levels (Mj = −1, 0, +1) excitation, which exhibits transition ($^7F_1 \rightarrow {}^5D_0$) between the $|k\rangle$ and $|l\rangle$ levels. Following the loop through the single excitation H_1 and de-excitation H_1^* (Fig. 1(b)) yields the out-of-phase FL signal H_{FL} is generated by following the closed loop through single excitation H_1 and de-excitation H_1^* Fig. 1(b). The in-phase SFWM Stokes H_S anti-Stokes H_{AS} signals are generated by following the closed loop under phase-matched condition $\boldsymbol{k} + \boldsymbol{k}' = \boldsymbol{k_S} + \boldsymbol{k_{AS}}$ produced by two excitations $H_1(\omega_1, k_1)$ and its reflection $H_1'(\omega, k_1')$ and one de-excitation $H_{S/AS}^*$ Fig. 1(b).

The spectral signals in Eu^{3+}: $BiPO_4$ crystals are obtained by varying the time GP and GW [35], using narrowband and broadband lasers (570 nm–610nm). Temporal profile is achieved by connecting these spectrums at different decay rates (ms) and GW (μs). The three PMTs are positioned at different polarization angles, i.e., PMT1 at 60°, PMT2 at 30°, and PMT3 at 35° ($\theta_1 > \theta_3 > \theta_2$) as shown in Fig. 1(c). In this experiment, we demonstrated that the H-phase (0.5:1) exhibits strong dressing quantization compared to (6:1), (12:1), (7:1) and (1:1) phase because of larger gamma phonons quantization and the phonon density of states, by controlling time gate width (GW), time gate position (GP), detecting angles, laser and power.

Both the FL and SFWM signals were produced in the same spectral range of the $^5D_0 \rightarrow {}^7F_1$ transition (570 nm-610 nm). Both signals were separated temporally throughout detection. The coherent SFWM signal, which was distinguished by its long decay scale, being detected at

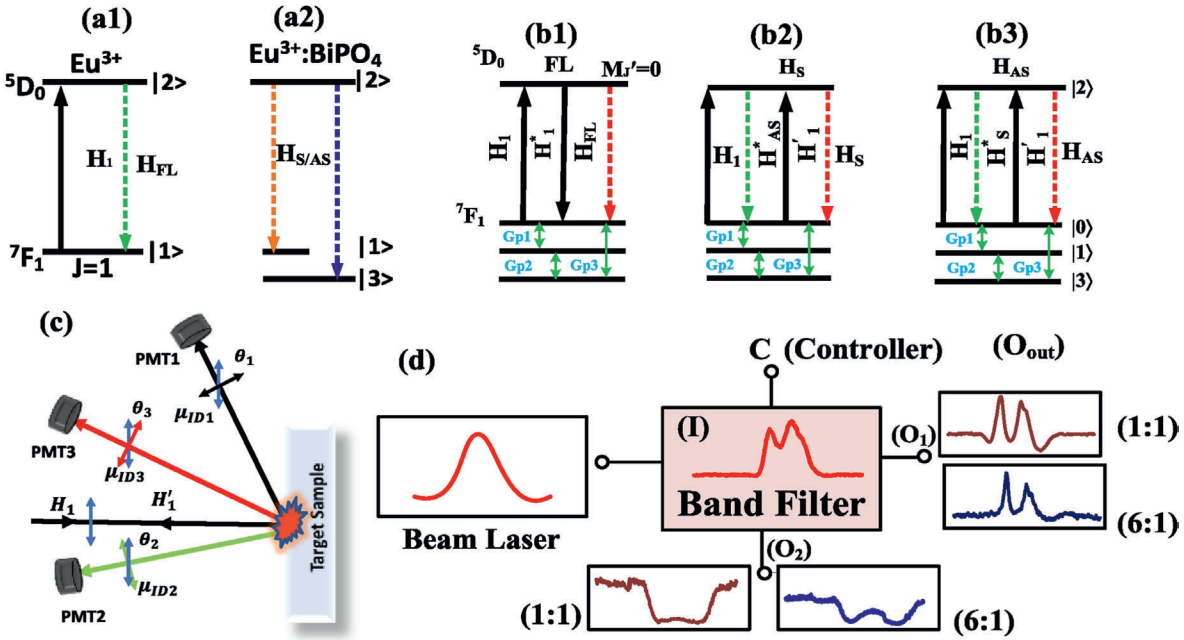

Fig. 1. Energy level of Eu3+ ion, Crystal field splitting of 7F1 energy level (b) Dressing assist CF quantization (c) Schematic diagram of emission and detection of the spectral signal at different polarization angles (PMT1(600), PMT2(300), PMT3(350)). (d) Band filter controlled by time gate width.

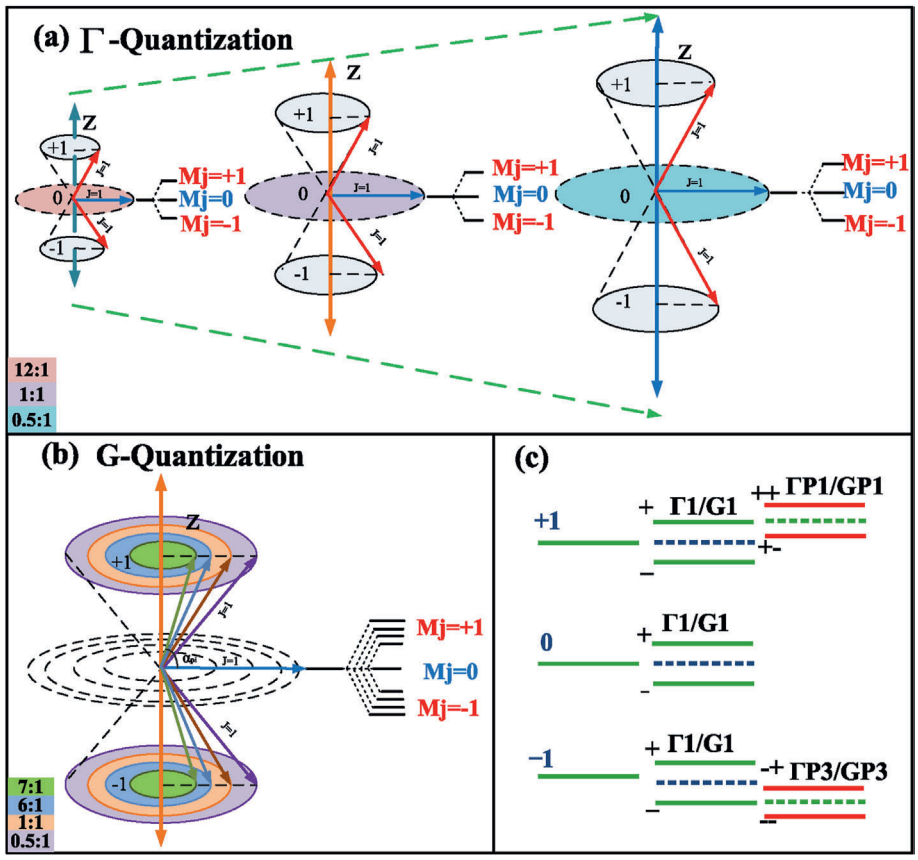

Fig. 2. Destructive quantization is larger than constructive quantization, (a) Different phase transition gamma destructive quantization, (b) Different phase transition G constructive quantization, (c) shows ground state 7F1 dressing sub-level for three CF levels.

increased GP and the incoherent FL signal, which was an instantaneous linear process, being captured at shorter GP. This time-gating approach permits the separation and independent investigation of these two quantum optical effects from the same system.

2.2. Phase transition quantization

2.2.1. Three-dimensional quantization for peak and dip signal

The interplay between photon-phonon dressing and crystal field quantization gave rise to phase transition in Eu^{3+}: $BiPO_4$. The phase transition quantization in Eu^{3+}: $BiPO_4$ is influenced by 2D and 3D quantization. Peak and dip quantization have two projections, with peak intensity and dip intensity projections in Fig. 2(a and b). The peak intensity along x-axis and dip intensity along y-axis. Three-dimensional dressing field quantization originates from the external field while two-dimensional crystal field quantization originates from stark field and produces external field quantum precession around the z-axis. This leads to the frequency shift (linewidth) along z-axis. The energy between levels and DOS is directly proportional to quantization in Fig. 2(a and b).

2.2.2. Five phase transition 2D quantization

Phase transition can be achieved through dressing assisted field quantization, which originates from laser and phonon fields along the z-axis in Fig. 2(a and b). In Eu^{3+}: $BiPO_4$, the quantization of $^7F_1$ leads to the splitting of energy levels in Fig. 1(b) respectively. Compared with 2D quantization, 3D quantization has an extra Y-axis. The DOS along Y-directional projection corresponds to peak. The DOS and dressing are inversely proportional to the frequency quantization gap, but they cannot coexist simultaneously. In general, external field quantum precession $\mu_E = -g\mu_o\ M_J$ makes quantization, which leads to the energy between levels along z-projection $\Delta E_Z = -g\mu_o\ M_J E\cos(\alpha_i + \alpha_{pi})$ in Fig. 2. Where α_i corresponds to laser field and α_{pi} responds to different phonon phase transition (12:1, 1:1, 0.5:1, 7:1, 6:1). The frequency splitting of 12:1 phase is smaller along z-axis as compared to 1:1 phase, while 0.5:1 phase exhibits the largest frequency splitting and largest DOS, which results strong gamma quantization in Fig. 2(a). However, 7:1 phase shows the smallest frequency splitting when compared to 6:1 phase, 1:1 phase, and 0.5:1 phase. The density of states in the 0.5:1 phase is the highest in G quantization in Fig. 2(b). 0:5:1 exhibits the strongest quantization due to large phonon density, while 12:1, 1:1. 7:1 shows weak quantization due to phonon density is small. In gamma quantization, 0:5:1 exhibits strongest quantization as compared to 1:1, 12:1 due to larger gamma phonon.

The dressing field quantization is caused by the laser field and phonon field along z-axis, which produces quantization of 7F1 in Fig. 2 (a2), which correspond to dressing sublevels in Fig. 2(c) for $\Gamma^i_{kl} \gg G^i$. The upward precession cone corresponds to three bright states (Fig. 2(b)) (++, +-, –), which originates from initial CF level ($m_J = +1$). The internal first bright state is from photon dressing $|\pm> = \sin(\theta_i)|0> \pm \cos(\theta_i)|2>$ and dark state $\Delta_1^+ = 0$ while external bright state is from phonon dressing $|\pm> = \sin(\theta_i + \theta_{pi})|+> \pm\cos(\theta_i + \theta_{pi})|1>$ and dark state $\Delta_{p1}^+ = \lambda_+^+$. For $G^i \gg \Gamma^i_{kl}$, have two dressing which corresponds to dressing sublevel in Fig. 2(c). The upward precession cone corresponds to three bright states (Fig. 2(b)) (++, +-, –), which originates from initial CF level $m_J = +1$. The internal first bright state is from photon dressing $|\pm> = \sin(\theta_i)|0> \pm\cos(\theta_i)|2>$ and dark state $\Delta_1^+ = 0$ while external bright state is from phonon dressing $|\pm> = \sin(\theta_i + \theta_{pi})|+> \pm \cos(\theta_i + \theta_{pi})|1>$ and dark state $\Delta_{p1}^+ = \lambda_+^+$. The frequency splitting (along z-axis) among three bright states and density of state (along x-axis) are determined by the photon-phonon dressing fields.

3. Theoritical model

CF quantization (DC-like) in Fig. 1(a2) has three energy level, like dressing assist CF quantization (AC-like) in Fig. 1 (a3). Moreover, CF quantization shows one directional level (|1>, |4>, |3>) response to (Mj = 0, +1, −1), and dressing assisted CF levels (|0>, |1>, |3>) response to (Mj = +1, 0, −1) respectively.

Two levels (|1>, |3>) remain the same for both quantization, however, the CF level |4> degenerate to |0> dressing assist CF level.

3.1. FL NON-HERMITIAN quantization and interaction IN Eu3+: BiPO4

AC quantization have three levels (+1,0, −1) while DC quantization have two levels (mj = -1, 0) which are overlapped with AC. So, DC have similar level but formula is different because dressing is different. In CF photon-phonon dressing is zero. But generation is not zero. The second order density matrix element FL AC-like quantization for Cascade double dressing case via perturbation chain $\rho_{00}^{(0)} \overset{H_1}{\rightarrow} \rho_{20}^{(1)} \overset{H_1^*}{\rightarrow} \rho_{22}^{(2)}$, $\rho_{33}^{(0)} \overset{H_1}{\rightarrow} \rho_{23}^{(1)} \overset{H_1^*}{\rightarrow} \rho_{22}^{(2)}$, $\rho_{11}^{(0)} \overset{H_1}{\rightarrow} \rho_{21}^{(1)} \overset{H_1^*}{\rightarrow} \rho_{22}^{(2)}$ can be written as.

$$\rho^0_{(\Delta m_J=0)} = \left|G_1^0\, cos(\theta_i)\right|^2 \Big/ \left(\Gamma^0_{21} + i\Delta_1^0 + \left|G_1^0 \times cos(\theta_i)\right|^2 \Big/ \left(\Gamma^0_{21} + i\Delta_1^0\right) + ... \right.$$
$$\left. ...\left|G^0_{p1} \times cos\left(\theta_i + \theta_{pi}\right)\right|^2 \Big/ \left(\Gamma^0_{01} + i\Delta_1^0 - i\Delta^0_{p1}\right)\right)\Gamma^0_{22} \tag{1}$$

$$\rho^{+(2)}_{FL(\Delta m_J=-1)} = \left|G_1^+\right| \Big/ \left(\Gamma^+_{20} + i\Delta_1^+ + \left|G_1^+ \times cos(\theta_i)\right|^2 \Big/ \left(\Gamma^+_{20} + i\Delta_1^+\right) + ... \right.$$
$$\left. ....\left|G^+_{p3} \times cos\left(\theta_i + \theta_{pi}\right)\right|^2 \Big/ \left(\Gamma^+_{30} + i\Delta_1^+ - i\Delta^+_{p3}\right)\right)\Gamma^+_{22} \tag{2}$$

$$\rho^{-(2)}_{S/AS(\Delta m_J=+1)} = \left|G_1^-\right|^2 \Big/ \left(\Gamma^-_{23} + i\Delta_1^- + \left|G_1^- \times cos(\theta_i)\right|^2 \Big/ \left(\Gamma^-_{23} + i\Delta_1^-\right) + ... \right.$$
$$\left. .....\left|G^-_{p2} \times cos\left(\theta_i + \theta_{pi}\right)\right|^2 \Big/ \left(\Gamma^-_{13} + i\Delta_1^- - i\Delta^-_{p2}\right)\right)\Gamma^-_{22} \tag{3}$$

III.1. SFWM AC & DC-like Quantization
III.2. Temporal Autler-Townes splitting

The temporal intensity of FL signal determines the TAT splitting which can be written in Eq. (7) via second-order FL density element.

$$\mathbf{I_{FL/S}} = \left|\boldsymbol{\rho}_{\mathbf{FL/S}}\right|^2 \left[e^{\mathbf{G^2 et^2}} \otimes \otimes + \mathbf{e}^{-\,(\mathbf{t}-\boldsymbol{\tau}_0)^2/2\mathbf{t}_p^2} \otimes \mathbf{e}^{\mathbf{tI\Gamma_S}}\right] \tag{7}$$

3.2. SFWM AC & DC-like quantization

AC quantization have three levels (+1,0, −1) while DC quantization have two levels (mj = -1, 0) which are overlapped with AC. So, DC have similar level but formula is different because dressing is different. In CF photon-phonon dressing is zero. But generation is not zero. The second order density matrix element FL AC-like quantization for Cascade double dressing case via perturbation chain $\rho_{00}^{(0)} \overset{H_1}{\rightarrow} \rho_{20}^{(1)} \overset{H_1^*}{\rightarrow} \rho_{22}^{(2)}$, $\rho_{33}^{(0)} \overset{H_1}{\rightarrow} \rho_{23}^{(1)} \overset{H_1^*}{\rightarrow} \rho_{22}^{(2)}$, $\rho_{11}^{(0)} \overset{H_1}{\rightarrow} \rho_{21}^{(1)} \overset{H_1^*}{\rightarrow} \rho_{22}^{(2)}$ can be written as.

$$\rho_{S/AS}^{+(3)} = i\left(G_{AS}^{+}\right)^{*} G + G' + \Big/ \left(\Gamma_{20}^{+} + i\Delta_{1}^{+}\right)\left(\Gamma_{00}^{+} + i\delta_{S/AS} + \left|G_{1}^{+} \times cos(\theta_i)\right|^2 \Big/ \left(\Gamma_{20}^{+} + i\delta_{S/AS} + i\Delta_{1}^{+}\right) + \left|G_{p3}^{+} \times cos\left(\theta_i + \theta_{pi}\right)\right|^2 \Big/ \left(\Gamma_{30}^{+} + i\delta_{S/AS} - i\Delta_{p3}^{+}\right)\right)\left(\Gamma_{20}^{+} + i\delta_{S/AS} + i\Delta_{1}^{+'}\right) \tag{4}$$

$$\rho_{S/AS}^{0(3)} = -i\left(G_{AS}^{0}\right)^{*} G^{0} G'^{0} \Big/ \left(\Gamma_{21}^{0} + i\Delta_{1}^{0}\right)\left(\Gamma_{11}^{0} + i\delta_{S/AS}\right) + \left|G_{1}^{0} \times cos(\theta_i)\right|^2 \Big/ \left(\Gamma_{21}^{0} + i\delta_{S/AS} + i\Delta_{1}^{0}\right) \ldots\ldots$$
$$\ldots\ldots + \left|G_{p1}^{0} \times cos\left(\theta_i + \theta_{pi}\right)\right|^2 \Big/ \left(\Gamma_{01}^{0} + i\delta_{S/AS} - i\Delta_{p1}^{0}\right)\Big)\left(\Gamma_{21}^{0} + i\delta_{S/AS} + i\Delta_{1}^{0'}\right) \tag{5}$$

$$\rho_{S/AS}^{-(3)} = -i\left(G_{AS}^{-}\right)^{*} G^{-} G'^{-} \Big/ \left(\Gamma_{23}^{-} + i\Delta_{1}^{-}\right)\left(\Gamma_{33}^{-} + i\delta_{S/AS}\right) + \left|G_{1}^{-} \times cos(\theta_i)\right|^2 \Big/ \left(\Gamma_{23}^{-} + i\delta_{S/AS} + i\Delta_{1}^{-}\right) \ldots\ldots$$
$$\ldots\ldots + \left|G_{p2}^{-} \times cos\left(\theta_i + \theta_{pi}\right)\right|^2 \Big/ \left(\Gamma_{13}^{-} + i\delta_{S/AS} - i\Delta_{p2}^{-}\right)\Big)\left(\Gamma_{23}^{-} + i\delta_{S/AS} + i\Delta_{1}^{-'}\right) \tag{6}$$

3.3. Temporal Autler-Townes splitting

The temporal intensity of FL signal determines the TAT splitting which can be written in Eq. (7) via second-order FL density element.

$$\mathbf{I_{FL/S}} = \left|\boldsymbol{\rho}_{\mathbf{FL/S}}\right|^2 \left[e^{G^2 et^2} \otimes\otimes + \mathbf{e}^{-(\mathbf{t}-\boldsymbol{\tau}_0)^{2/2\tau_p^2}} \otimes\right] \tag{7}$$

4. Experimental results

The experimental part of this paper consists of four sections, which are classified as destructive gamma phonon quantization at FL region in three different phases (12:1, 1:1, 0.5:1) of Eu^{3+}: $BiPO_4$ (Fig. 3); phonon quantization with TAT and SAT splitting at FL region in 6:1 phase (Figs. 4 and 5); constructive frequency phonon quantization in SFWM region in four different phases (7:1, 6:1, 1:1, 0.5:1) (Fig. 6); phonon quantization with single and two-laser FL destructive dressing interactions in 12:1 phase of Eu^{3+}: $BiPO_4$ (Figs. 7 and 8).

4.1. Destructive gamma phonon quantization for phase transition of Eu^{3+}: $BiPO_4$

Fig. 3 shows destructive gamma phonon quantization by comparing three different phases (12:1, 1:1, 0.5:1) of Eu^{3+}: $BiPO_4$ by changing the time gate position (GP) at different quantization angles through narrowband excitation at fixed time gate width (600 ns). Small angle (PMT2) spectrums (Fig. 3(a1, b1, c1)) show peaks (weak dressing), while large angle (PMT1) spectrums (Fig. 3(d1, e1, f1)) show dips (strong dressing). To explain this exceptional phenomenon, we introduce destructive quantization. According to angle quantization theory, $\Delta E_Z = -g\mu_o\ m_J E_i \cos(\theta_l)$ small angle exhibits more dressing Rabi frequency $\left|G_1^i\right|^2/\left(\Gamma_{kl}^i + i\delta_{S/AS} - i\Delta_1^i\right)$ in Eqs. (1)–(3). The experimental results are inversely proportional to the theory. So, compared with Fig. 3 (a, b, c), Fig. 3(d, e, f) shows the destructive angle quantization due to Γ_{FL}^i increasing. Moreover, increasing GP follows the time decay curve. Changing GP brings transformation in Γ_{FL}^i quantization by selecting different level, where a notable change in signal can be observed. Increasing GP also make decrease in out-of-phase ($\left(\Gamma_{FL}^i \cong G_1^i\right)$) and results in CF splitting in Fig. 3(d4-d6, e4-e6, f4-f6). At GP (500 ns) PMT2 spectrums show broad peaks for all phases (12:1, 1:1, 0.5:1) in Fig. 3(a1, b1, c1) due to weak phonon Γ_{FL}^i quantization (G dominant). The weakest dressing dips along broad peak can be seen in Fig. 3 (a). By increasing GP (800 ns), the intensity of broad peaks decreases in Fig. 3 (a2 and c2), however broad peak converted to narrow peak with increased intensity in Fig. 3(b2). For this change in Fig. 3(a2, b2 and c2), the Γ_{FL}^i quantization become weaker. By increasing more GP(1 μs), the peaks intensity

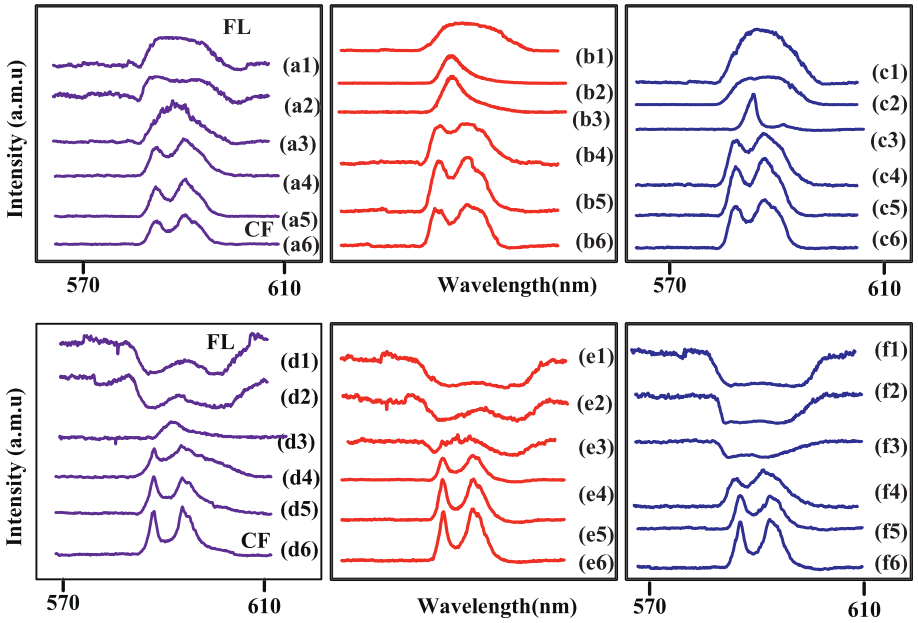

Fig. 3. Shows spectral signal comparison of Eu^{3+}: $BiPO_4$ for three phases (12:1, 1:1, 0.5:1) at high power (9 mW) through narrowband excitation by changing time gate position GP (500 ns, 800 ns, 2 μs, 5 μs, 10 μs, 15 μs), with fixed time gate width (600 ns), (a) (b) (c) at small angle (300) PMT2 while (d) (e) (f) at large angle PMT1 (600) of (12:1, 1:1, 0.5:1), respectively.

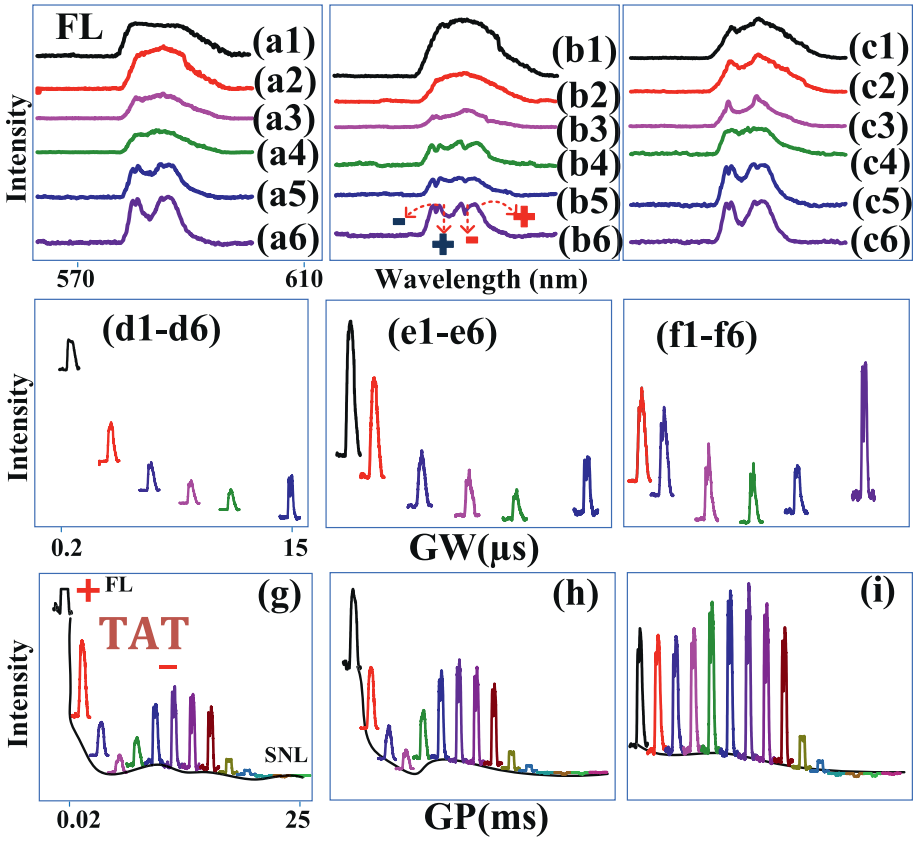

Fig. 4. Shows spectral and temporal intensity from half HP and half LTMP (6:1) of Eu^{3+}: $BiPO_4$ through broadband excitation at room temperature and high power at smaller angle (300), (a, b, c) shows overlapping spectral signal at changing GW = 200ns-15 μs while GP is fixed (1ns,500ns,1 μs), respectively. (d, e, f) is connecting figures of (a, b, c) respectively. (g, h, i) shows the spectral-temporal signals at changing GP (200 ns?25 ms) with fixed GW (200ns,1 μs,15 μs), respectively.

become increase (increasing G) in Fig. 3(a3, b3, c3), however the linewidth in Fig. 3(a3) is much greater than Fig. 3(b3, c3). By increasing GP (5us-15 μs), the highest peak intensity split in two distinguish dips (CF) in Fig. 3(a4-a6, b4-b6, c4-c6), where Γ^i_{FL} and G quantization become equal $(\Gamma^i_{FL} \cong G^i_1)$. At PMT1 near GP (500 ns) the (1:1 and 0.5:1) phases spectrums have broad dips in 3(e1 and f1), however (0.5:1) has the strongest dressing and (12:1) has two dips in Fig. 3(d1) because of strong phonon Γ^i_{FL} quantization exists. The strongest destructive quantization can be observed in (0.5:1) phase in Fig. 3(f1). By increasing GP (800 ns), gamma quantization decreases and the dressing in Fig. 3(d2, e2, f2) decreases. More increasing GP(1 μs), the G effect increasing and two dressing dips convert to weak peak in Fig. 3(d3), however in Fig. 3(e3) weak peak-dips is obtained. But in Fig. 3(f3) remain dressing dip. Increasing GP(5us-15 μs), all the phases 3(d4-d6, e4-e6, f42-f6) show two distinguish peaks (CF splitting), because the G effect increases and equal to gamma quantization. The turning point (CF splitting) in all Fig. 3(d4, e4, f4) appears at same time. Also, we observed at PMT2, all phases show CF quantization at same point (Fig. 3(a4, b4, c4)). The transition between ground state 7F1 sublevels and excited state 5D0 with six sub-levels is in Fig. 3(f1). There exist six bright states and four dark states from CF level $(Mj = -1, 0, +1)$, which results from photon-phonon dressing. Further, the dressing sub-levels for Fig. 2(c1) are explained (See Supplementary). In Fig. 3(e1) destructive dressing exhibits four dressing, which already explained in Fig. 3(d1). The five dressings correspond to Fig. 3(f1) are explained (See Supplementary). By comparing different phases (12:1, 1:1, 0.5:1), we concluded that in Fig. 3 at larger angle, the (0.5:1) phase has more destructive quantization as compared to (12:1, 1:1), while at small angle, (12:1) has more constructive quantization than (0.5:1, 1:1) in FL region.

4.2. Destructive quantization with TAT and SAT splitting

Fig. 4 shows SAT splitting and TAT dressing quantization at PMT2 by changing GW and GP of H = M phase (6:1). At GW = 200 ns, PMT2 spectrums in Fig. 4(a1) shows broad peaks at GP (1 ns) obtained by weak Γ^i_{FL} quantization. Increasing GW (800ns-1us), the spectrum peak intensity in Fig. 4(a2-a4) become weaker due to gamma decreased. Increasing GW (5us-15 μs) further, multi-level out-of-phase destructively interfere each other, and weak peak converted to CF splitting along small SAT splitting exists in Fig. 4(a5-a6). The Γ^i_{kl} quantization led the weak destructive dressing to SAT splitting evolution, where, gamma is almost equal G (G dominant). An increase in GP = 500 ns at GW = 200 ns, a broad peak is obtained in Fig. 4(b1) because of weak gamma quantization. Increasing GW (800ns-1us) causes decrease in gamma quantization and the spectrum peak intensity become weaker in Fig. 4 (b2-b3). Increasing GW (5us-15 μs), the weaker peak shows SAT splitting in Fig. 4(b4-b6) where G is larger than gamma quantization. More increase in GP (1 μs), broader peak is shifted into two weak peak due to GP increase shows in Fig. 4(c1). Increase in GW (800 ns), two peaks intensity reached to near CF splitting in Fig. 4(c2), where G is almost equal to gamma (gamma dominant). Increasing GW = 1 μs decrease the gamma quantization and results in CF splitting (Fig. 4(c3)), where gamma become equal to G. Increasing GW(5us-15 μs), increase Rabi frequency (G), and CF splitting shows small SAT splitting in Fig. 4(c5-c6).

In Fig. 4(c3), CF splitting occurs earlier compared to Fig. 4(a3, b3). At small GP, weak gamma quantization is observed at small angles. As GP increases, gamma quantization weakens further, leading to earlier CF splitting. The time GW variation in (Fig. 4(a–c)) shows the evolution from out-of-phase (FL) weak dressing to in-phase constructive AT splitting in Fig. 4(a5-a6, b4-b6, c5-c6).

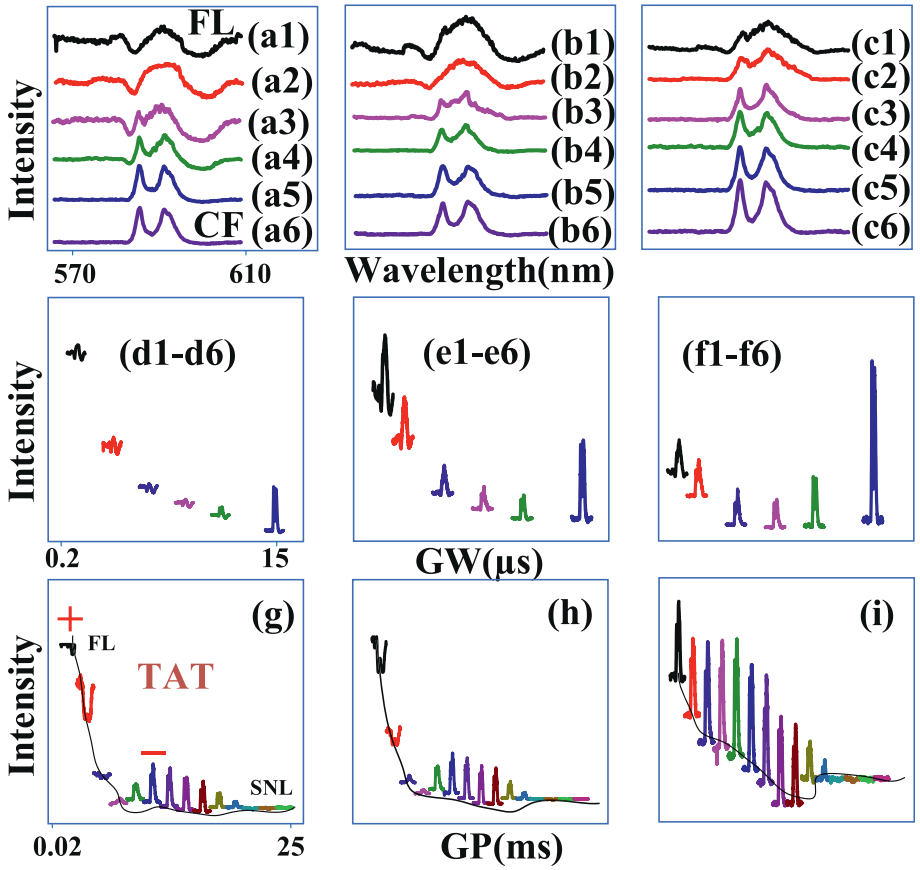

Fig. 5. Shows spectral and temporal intensity from half HP and half LTMP (6:1) of Eu^{3+}: $BiPO_4$ through broadband excitation at room temperature and high power at larger angle (60°), (a, b, c) shows overlapping spectral signal at changing GW = 200ns-15 μs while GP are fixed (1ns,500ns,1 μs), respectively. (d, e, f) is connecting figures of (a, b, c) respectively. (g, h, i) shows the spectral-temporal signals at changing GP (200ns-25 ms) with fixed GW (200ns,1 μs,15 μs), respectively.

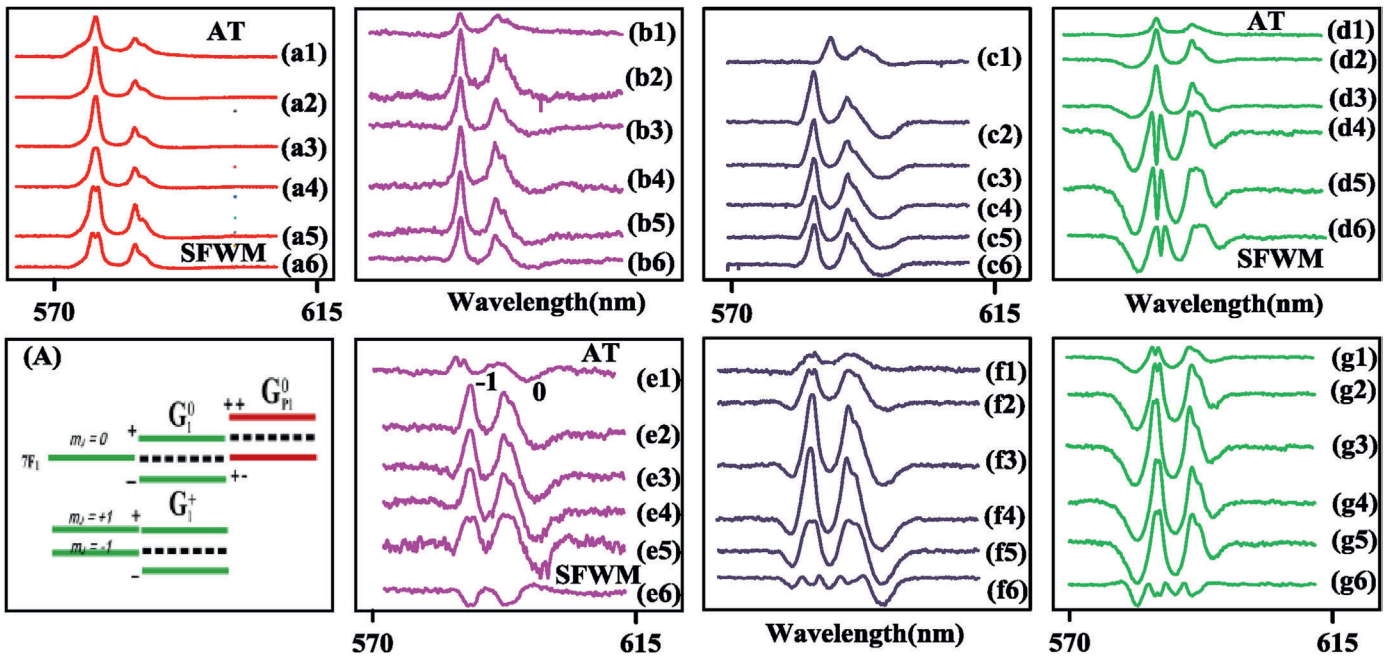

Fig. 6. Shows broadband spectral comparison of four different phases (7:1, 6:1, 1:1, 0.5:1) at high power (9 mW) by changing time GP (20us-500 μs) at fixed time GW (500 ns), (a, b, c, d) at PMT1(60°) of (7:1, 6:1, 1:1, 0.5:1), respectively, while (e, f, g) at PMT2(30°) of (6:1, 1:1, 0.5:1), respectively. (A) Shows sub-level of (7:1) ground state ($^7F_1$).

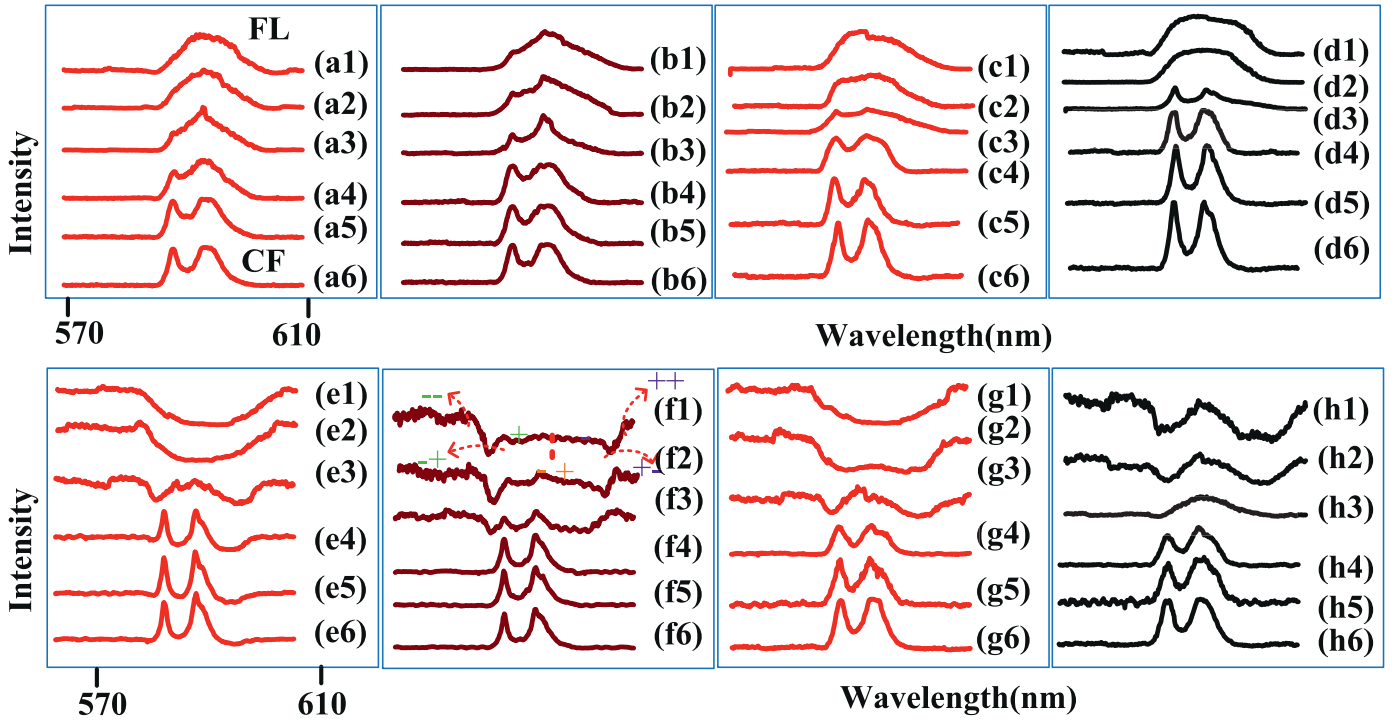

Fig. 7. Shows narrowband spectral signal of Eu3+: BiPO4 (12:1) phase at room temp and high power (9 mW) (a, b, c, d) at PMT2 and (e, f, g, h) at PMT1, (a, b, e, f) changing TGW= (500ns- 15 μs) at fixed TGP= (500 ns, 1.5 μs), while, (c, d, g, h) changing TGP= (500ns-15 μs) at fixed TGW= (200 ns, 1 μs).

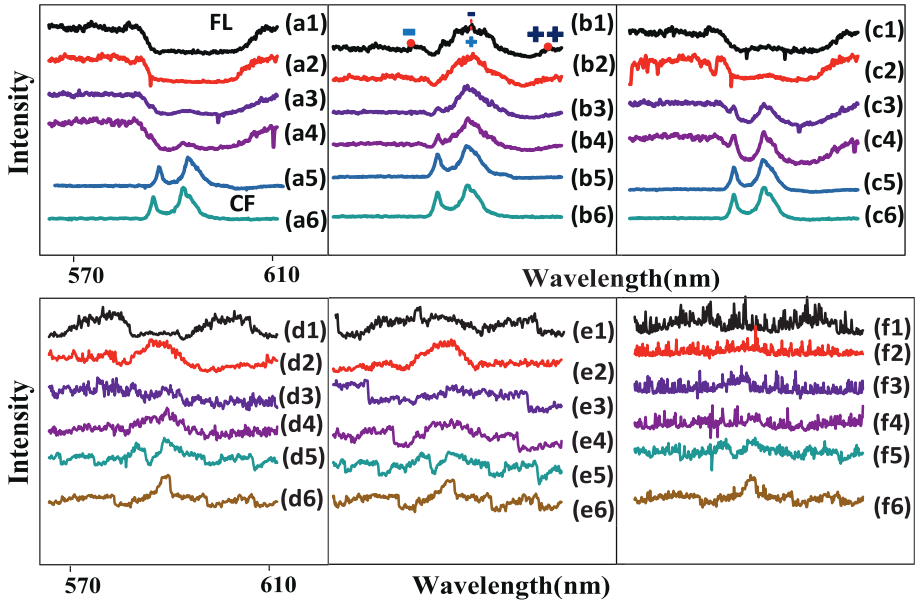

Fig. 8. Shows dual laser interaction profile with single laser spectral signal observed for (12:1) phase Eu^{3+}: $BiPO_4$ through narrowband laser is scanned from 575 to 610 nm while broadband is fixed at 552 nm at room temp and high power (9 mW) by changing GW (500ns-15 μs) at fixed GP = 200ns. (a, b, c) single laser (narrowband) and (d, e, f) two lasers interaction. (a, d), (b, e) and (c, f) at PMT1 (60°), PMT2 (30°) and PMT3 (35°) respectively.

The connecting Fig. 4(d, e, f) correspond to the spectral Fig. 4(a, b, c) respectively. Non-resonance in Fig. 4(d) shows out-of-phase. However, non-resonance in Fig. 4(e) initially shows weak out-of-phase to turning point (Fig. 4(e5), while in Fig. 4(f) non-resonance initiated with weak out-of-phase along small in-phase (Fig. 4(c5-c6)).

Based on resonance, the connecting temporal profile (Fig. 4(g and h) show a splitting gap between Fig. 4(g1-g7, h1-h7), with a time delay ranging from 0.2μs to 15 μs, known as Temporal Autler-Townes (TAT) splitting. This TAT (Fig. 4(g and h)) corresponds to the difference between dressing sub-level splitting ++ of CF level + and – of CF level - in Fig. 2(c). Moreover, The TAT splitting depends on the relationship between gamma and G, stronger TAT observed when gamma is closer to G, as shown in Fig. 4(h) at GW (1 μs), as compared to Fig. 4(g) at GW (200 ns) where gamma is greater than G. In contrast, Fig. 4(i) does not exist TAT because of greater G at GW (15 μs).

We concluded increasing GW (more multi-level interfere each other) leads the weak dressing peak to SAT splitting at smaller angle of (6:1) phase. In Fig. 4(b) has strong SAT splitting because of larger Rabi

frequency at GP = 500ns. The weak in-phase non-resonance baseline appears at far GP. Strong TAT is observed in Fig. 4(h) which relates with strong SAT (caused dominant G) in Fig. 4(b). In next figure, results will compare at larger angle under the same conditions.

Fig. 5 shows CF splitting and TAT evolution at larger angle (PMT1) with the same conditions as in Fig. 4. By comparing angles spectrums in Fig. 5(a1, b1, c1), PMT1 has stronger dressing than PMT2 in Fig. 4(a1, b1, c1). According to angle quantization theory explained above in Fig. 3, small angle exhibits larger Rabi frequency. But the experimental results obtained in Figs. 4 and 5 are opposite to the theory. So, (6:1) phase has angle destructive gamma phonon quantization.

At GW = 200ns and GP = 1 ns, PMT1 shows two dressing dips with peak in Fig. 5(a1) with strong gamma quantization. Increasing GW (800ns-1us), the two dressing dips become weaker along with broad peak in Fig. 5(a2-a3) by decreasing gamma quantization. More increasing GW (5 μs) causes more decreasing gamma and the spectrum converts into two distinguish peaks in Fig. 5(a4). Increasing GW (10us-15 μs), two peaks converted to CF splitting in Fig. 5(a4-a6), where multi-levels destructively interfere and (G = gamma). Increasing GP (500 ns) at GW = 200ns in Fig. 5(b1) shows two weak dressing dips with broad peak because increase in GP reduce the gamma quantization and two dressing dips become weaker. Increasing GW (800 ns), the weak dressing dips disappear and converted to broad dip in Fig. 5(b2) by weaker gamma quantization. Increasing GW(1 μs) the broad peak split into two peaks in Fig. 5(b3) where G is closer to gamma quantization and then convert to CF (G equal to gamma) in Fig. (b4-b6). Increasing GP more (1 μs), PMT1 at GW = 200ns shows broad peak in Fig. 5(c1) due to weakest gamma quantization. The broad peak split in two peaks at GW = 800ns in Fig. 5(c2) because of G effect increasing. More increasing GW (1us-15 μs), two peak intensity increases and convert to CF splitting in Fig. 5(c3-c6).

We observed that increasing GP and GW reduce the gamma quantization which effect on spectral behavior. Increasing GW, Fig. 4 favors SAT splitting from broad peak because of strong G at small angle, while, in Fig. 5(a–c) larger angle shows multi-dips evolving into CF quantization, where G is equal to gamma quantization, highlighting the angle as a key factor in spectral behavior. At fixed GW (1 μs), varying GP (1 ns, 500 ns, 1μs) in Fig. 5(a3, b3, c3) show distinct spectral evolution i.e broad peaks with weak dressing in Fig. 5(a3), two peaks in Fig. 5(b3), and CF splitting in Fig. 5(c3). These results demonstrate how GP changing modulates gamma quantization.

The connecting Fig. 5(d, e, f) correspond to the spectral Fig. 5(a, b, c) respectively. Non-resonance in Fig. 5(d) shows strong out-of-phase. However, non-resonance in Fig. 5(e and f) initiate with out-of-phase and become flat. However, turning point reach earlier in Fig. 5(f4). The connecting temporal profiles in Fig. 5(g, h, i) exhibit much weaker TAT compared to Fig. 4(g, h, i). This weakening is caused by larger angle-induced gamma quantization in the FL region, which suppresses TAT. As a result, TAT is significantly reduced in Fig. 5(g and h) as compared to Fig. 4(g and h), while did not show TAT in Fig. 5(i).

We concluded that (6:1) phase shows angle destructive gamma quantization in FL region. Small angle at far GP = 1 μs in Fig. 4(f5-f6) shows stronger non-resonance in-phase, while larger angle does not exhibit in-phase (Fig. 5(f5-f6) due to more Rabi frequency at small angle. Stronger TAT is shown at small angle in Fig. 4(g and h) having less gamma phonon quantization. Moreover, larger angle of (6:1) phase in Fig. 5 has weak destructive gamma phonon quantization compared to the (1:1, 12:1 and 0.5:1) phase in Fig. 3. The (0.5:1) in Fig. 3 exhibits stronger phonon gamma destructive quantization than (6:1) phase. In next figure, quantization will discuss in SWFM region for different phases. A band pass filter is a type of filter that only allows signals to go through of specific range frequency. Using unique properties of filter, it eliminates undesirable frequencies. It is useful in wireless communication systems and remove noises or interference. Our designed band pass filter is made to enhance signal clarity, remove unwanted frequencies and efficiency in wireless communication system, as shown in Fig. 1(d). The main principal of this special designed filter is to convert signal arising from crystal field (acting as input (I)) into multi peaks-dips (output O1) called multi-channel filter, while, broad dressing dips (output O2) known as band pass filter. The important characteristics of this filter is to generate multi peaks-dips and broad dip (Figs. 3 and 6) by adjusting the different phases of Eu3+: BiPO4 crystal at specific GP and GW facilitated by a control knob labelled C (photon-phonon dressing). Moreover, the filter allows control over the selectivity of outputs (O1, O2) by adjusting the de-phase rate Γ^{i}_{kl} and phonon dressing Rabi frequency. The theoretical structure of this designed diode is derived from the results depicted in Fig. (3 and 6). Meanwhile, by using the bandwidth formula (BW= (λca - λcb)/(λca+ λcb) *100 %) the efficacy of the band pass filter is quantified through the computation of phase quantization for two different phases (1:1 and 6:1) of Eu3+: BiPO4, yielding percentages of 10 % and 14.5 %, respectively.

4.3. Constructive frequency phonon quantization

Fig. 6 shows constructive quantization and phonon density of state of four different phases (7:1, 6:1, 1:1 and 0.5:1) by changing GP at different angles in SFWM region. Small angle (PMT2) spectrums (Fig. 6 (e6, f6, g6)) show stronger dressing dips as compare to larger angle (PMT1) spectrums (Fig. 6(b6, c6, d6)). So, experimental results in Fig. 6(b–g) are directly explained by the angle quantization formula $\Delta E_Z = -g\mu_o\ m_J E_i \cos(\theta_l)$ and dressing terms $\left|G^{i}_{1}\right|^2/\left(\Gamma^{i}_{kl} - i\Delta^{i}_{1} + i\delta_{AS/S}\right)$ $(i = -1, 0, +1)$ in eqs. (4)–(6). By comparing with Fig. 6(b, c, d), Fig. 6(e, f, g) exhibits constructive angle quantization due to phonon density rabi frequency increasing in SFWM region.

All spectrums shown in Fig. 6(a–g) have linear and circular quantization. Both quantization can transform by varying time GP. At GW = 500 ns, GP = 20 μs (near SFWM region), the (7:1) phase spectrum at PMT1 shows two peaks (linear and circular) due to weak phonon density in Fig. 6(a1). Increasing GP (80us-500 μs), both linear and circular quantization increases in Fig. 6(a2-a6) due to phonon density increases because of more photon-phonon interaction in this region. This means increasing phonon density has no significant effect on (7:1) phase. In contrast, the (6:1) phase spectrums in Fig. 6(b1-b2) also shows linear and circular peaks at GP (20us-80 μs) due to weak phonon density. By increasing GP (100 μs) in Fig. 6(b3), the phonon density become larger and weak linear dressing is observed, While, circular dressing is negligible because of $G^{-}_{1} \cong \Gamma^{-}_{+1/2}$. Increasing Furthermore, increasing GP (200μs–500 μs) in Fig. 6(b4-b6) the weak linear dressing remains constant and do not any significant change. Moreover, the phase (1:1) shows the same phenomenon in Fig. 6(c1-c6) as (6:1) phase in Fig. 6(b1-b6). However (1:1) has stronger phonon density, so (1:1) exhibits stronger linear dressing in Fig. 6(c2-c6) as compare to (6:1) phase in Fig. 6(b3-b6). Furthermore, the phase (0.5:1) in Fig. 6(d1-d2) exhibits two peaks same as in Fig. 6(b1-b2). Increasing GP = 100 μs, the circular dressing become stronger than the linear dressing in Fig. 6(d3). The nested phonons make circular dressing stronger and minimize the linear photon with a very weak dressing dip. By increasing GP (100us-500 μs) in Fig. 6 (d4-d6) shows strong left circular dressing and weak right circular dressing due to $G^{-}_{1} \gg \Gamma^{-}_{+1/2}$, $G^{+}_{1} > \Gamma^{+}_{+1/2}$. By comparing increasing GP, different phases at PMT1 (7:1, 6:1, 1:1 and 0.5:1), the (0.5:1) has strong dressing due to strong phonon density rabi frequency. So, (0.5:1) has strong dressing than other phases, While, (7:1) has weakest dressing at PMT1.

On the other hand, the phase (6:1) spectrum at PMT2 in Fig. 6(e1) shows peak with weak dip due to weak phonon density. Increasing GP (80μs–400 μs) causes increase in phonon density shows strong linear dressing ($G^{0}_{1} \gg \Gamma^{0}_{+1/2}$) and weak circular constructive quantization $G^{-}_{1} > \Gamma^{-}_{+1/2}$ in (Fig. 6(e2-e5)). Further at GP (500 μs) shows dips at circular quantization due to strong hyperfine gamma quantization $G^{-}_{1} \gg \Gamma^{-}_{+1/2}$ in Fig. 6(e6). The (1:1) phase in Fig. 6(f1) shows two weak dressing peaks

as in Fig. 6(e1). Increasing GP (80μs–400 μs) shows stronger linear dressing ($G_1^0 \gg \Gamma_{+1/2}^0$) and weak circular constructive quantization $G_1^- > \Gamma_{+1/2}^-$ in (Fig. 6(f2-f5)) than in (Fig. 6(e2-e5)), because (1:1) has larger number of phonon density, which increase rabi frequency. However, the hyperfine gamma quantization makes multi dips at larger GP (500 μs) in Fig. 6(f6). The (0.5:1) phase shows initially strong circular and very weak linear dressing in Fig. 6(g1). The circular dressing become stronger with increasing GP (80 μs–500 μs), while linear dressing is still weak in Fig. 6(g2-g5). Further at GP (500 μs) shows strong circular quantization due to hyperfine gamma quantization $G_1^- \gg \Gamma_{-1/2}^-$ in Fig. 6(g6).

H-phase (0.5:1) has higher phonon density of states [19] results in larger phonon dipole $\left(\mu_{pl}\right)$, which leads to a larger phonon Rabi frequency $\left(G_{pl}^i\right)$. The H-phase exhibits strong dressing as compare to (M-phase (7:1), H-M phase (1:1) and H = M phase (6:1)). Analysis revealed that larger phonon density of states in H-phase is characterized by high dressing. The H-M phase display relatively less phonon density of states response compared to H-phase. The H = M phase demonstrated comparable phonon coexist of both H and M phases. M-phase exhibited smaller phonon density of states, indicating pure M-phase exhibits weak dressing. Therefore, we concluded that H-phase has larger phonon density of states and exhibits more dressing. Thus, the H-phase has larger gamma quantization (five-dressing) with broader linewidth (24 nm), as shown in Fig. 3(f1), compared to the constructive G quantization (three-dressing) with linewidth (20 nm), shown in Fig. 6(g2). H-phase shows strong gamma destructive quantization in Fig. 2(a) and constructive quantization in Fig. 2(b).

We concluded that H-phase (0.5:1) shows strong constructive quantization due to more phonon density of state at both smaller and larger angles in SWFM region. While, M-phase (7:1) with less phonon density exhibits weak constructive quantization in SWFM region.

4.4. Phonon quantization with single and two-laser FL destructive dressing interaction

Fig. 7 shows destructive gamma phonon quantization of (12:1) phase at different time GP, GW and quantization angles through narrowband excitation in FL region. The (12:1) shows angle destructive quantization as already discussed in above Fig. 3(a–d). In Fig. 7, comparison of spectrums evolution can be observed by changing GP and GW. At GP = 500 ns, in FL region (GW = 500ns-2us) at PMT2 spectrum in Fig. 7(a1-a3) has broad peak because of weak gamma quantization. Increasing GW = 5us-15 μs leads to CF quantization in Fig. 7(a4-a6), where multi-level interferes each other. While increasing GP (1.5 μs), the broad peak is observed in Fig. 7(b1) at GW = 500 ns, and gamma is weaker by increasing GP. Increasing GW = 1us-15 μs shows the same phenomenon in Fig. 7(b2-b6) as in Fig. 7(a2-a6) that is leading to CF quantization, however at GP (1.5 μs) two peaks earlier appear in Fig. 7(b3) because increased GP make the out of phase weak. In contrast, at GP = 500ns in FL region (GW = 500ns-1us), PMT1 shows strong dressing dip in Fig. 7 (e1-e2) because larger gamma quantization ($\Gamma_{kl}^i \gg G^i$) exhibits. The strong dressing dip (Fig. 7(e1)) gradually become weaker and evolved to two dips along peak (Fig. 7(e3)) with increasing GW (2 μs) as multi-level interfere each other and make out of phase weak. More increasing GW = 5us-15 μs leads to CF quantization in Fig. 7(e4-e6), because multi-level interferes each other and gamma become equal to G quantization. Increased GP (1.5 μs) brings change in strong dressing dip (Fig. 7(e1)) to multi dips alignment in Fig. 7(f1) at GW = 500 ns, because the gamma quantization decreases. Increasing GW = 800ns-2us the multi-dips alignment converts into multi peak-dips in Fig. 7(f2-f3) due to gamma decreases. The multi peak-dips are evolved into CF splitting is observed in Fig. 7(f4-f6) with increasing GW (5us-15 μs) where multi-level out of phase completely balances each other. According to dressing sub-levels, the broad dip in Fig. 7(f1) can be explained by four destructive dressing 7(f1-f2) already explained above. One the other side fix GW = 200ns in FL region (GP = 500ns-2us) at PMT2 spectrum in Fig. 7(c1-c3) has broad peak because gamma quantization is weaker at small angle. Increasing GP = 5us-15 μs leads to CF quantization in Fig. 7(c4-c6), because gamma quantization decreases and become equal to G. An increase in GW (1 μs), the broad peak in Fig. 7(c1) become more increase in Fig. 7(d1) due to gamma quantization weaker at GP = 500ns. Increasing GP = 1us-15 μs gamma quantization come close to G and the peak split in two peak (Fig. 7(d3)) and then goes to CF (Fig. 7(d4-d6) where gamma quantization is equal to G. In contrast, PMT1 at GW = 200ns in FL region (GP = 500ns-1us) larger gamma quantization exhibits, where spectrums have dressing dips in Fig. 7(g1-g2). Increasing GW (2 μs), the strong dressing dip become weaker and evolved to two dips along peak (Fig. 7 (g3)), as multi-level interferes each other and make out of phase weak. More increasing GW = 5us-15 μs leads to CF quantization in Fig. 7(g4-g6). Increased GW (1 μs) decrease dressing and change the broad dressing dip (Fig. 7(g1)) into two dressing dips in Fig. 7(h1-h2) at GP = 500ns–800 ns? Increasing GP = 2 μs the two dips dressing converts into multi peak-dips in Fig. 7(h3) where gamma is closer to G. The multi peak-dips are evolved into CF splitting is observed in Fig. 7(h4-h6) with increasing GP (5us-15 μs).

We conclude that in FL region changing GP at fix GW or changing GW at fix GP has almost same effect i.e leading to CF quantization from broad peak at small angle and from strong dressing dip at large angle. (12:1) phase in Fig. 7(g) has mixture ratio (51 % HP + 49 % MP), so it has low asymmetry with more level splitting (strong dressing) as compare to (6:1), (7:1) in Figs. 5 and 7(a), respectively. However (12:1) has less level splitting as compare to (0.5:1) and (1:1) in Fig. 3. So, we conclude that in FL region (12:1) is more destructive as compare to (6:1), (7:1) but it is constructive than (0.5:1) and (1:1) which is already discussed in Fig. 3. In next figure, two laser behaviors in FL region for (12:1) phase will compare with single laser.

Fig. 8 shows the comparison of (12:1) phase of single laser and two lasers destructive dressing interactions in FL and AT region. Single laser spectrums show broad dips at larger angles (PMT1, PMT3) in (Fig. 8(a1-a2, c1-c2)) because of strongest Γ_{FL}^i quantization at GP = 200ns and GW = 500ns–800ns. Increasing GW (1us-15 μs), leads the dip alignment to CF splitting (Fig. 8(a5-a6, c5-c6)). The smaller angle PMT2 spectrum (Fig. 8(b1-b2)) shows two dips with peak at GP = 200 ns, GW = 500ns–800ns because of weak Γ_{FL}^i quantization. Increasing GW (1us-15 μs) the peaks converted into CF splitting (Fig. 8(b5-b6)). The single laser shows angle destructive quantization in FL region as we discussed in Fig. 7.

Fig. 8(d1) shows weak dressing dip due to two destructive dressing (G1 and G2) interaction from Eq. (3). This destructive dressing interaction can be controlled by the dressing angle (α) in the cross term $\left(\left|G_1^{(2)}\right|\left|G_2^{(2)}\right|\cos(\alpha)\right)$. A destructive dressing interaction is observed when ($\alpha = \pi$) as depicted in Fig. 2(b) [36]. When the TGW increases in Fig. 8 (d2)), the destructive interaction is reduced due to reduction in dressing angle $\pi/2<\alpha<\pi$. Further, increasing the time gate width, the destructive dressing is vanished due to dressing angle become $\pi/2$ in Fig. 8(d3-d6). However, at small angle in Fig. 8(e1-e6), the destructive quantization is reduced due to reduction in two dressing angles $\alpha = 5\pi/6$, $\left|G_1^{(2)}\right|\left|G_2^{(2)}\right|\cos(\alpha) < 0$. Furthermore, at large angle angle PMT 3 in Fig. 8 (f1-f6), the destructive dressing is completely vanished. We concluded that in Fig. 8(a–c) single laser shows strong dressing dips while two laser interaction shows weak dressing (negligible) because of additional laser.

5. Conclusion

In summary, this study depicted that non-Hermitian phonon destructive gamma quantization controlled through different phases of Eu3+: BiPO4. In atomic like system different phases can be regulated by key parameters (GW, GP, quantization angle, power and bandwidth). We studied that H-phase (0.5:1) has strongest dressing and shows more destructive quantization at larger angle because larger gamma exists,

while more constructive at small angle due to G in FL region. Angle destructive quantization is observed in (6:1) phase. Also, Strong TAT and SAT splitting has been investigated in FL region in (6:1) phase. Larger phonon density of state is studied in H-phase (0.5:1) as compared to M-phase (7:1), where H-phase (0.5:1) shows strong constructive quantization in SWFM region. Moreover, (12:1) phase has angle destructive quantization in FL region. Also, single-laser result in strong destructive dressing compared to two-laser interactions in (12:1) because additional laser cancels the gamma quantization effect.

CRediT authorship contribution statement

Muhammad Qasim Khan: Writing – original draft, Resources, Investigation, Data curation. **Iqbal Hussain:** Writing – review & editing, Visualization, Validation, Software. **Faisal Nadeem:** Software, Resources, Data curation. **Nadir Khan:** Visualization, Resources, Investigation. **Mudassir:** Resources, Investigation, Data curation. **Huanrong Fan:** Writing – review & editing, Writing – original draft, Supervision, Conceptualization. **Changbiao Li:** Visualization, Supervision, Funding acquisition. **Yanpeng Zhang:** Project administration, Methodology, Funding acquisition, Formal analysis, Conceptualization.

Declaration of competing interest

The authors declare that they have no known competing financial interests or personal relationships that could have appeared to influence the work reported in this paper.

Acknowledgments

This work was supported by the National Natural Science Foundation of China (62475208, 62475209, 12474392).

Appendix A. Supplementary data

Supplementary data to this article can be found online at https://doi.org/10.1016/j.pnsc.2025.09.007.

Data availability

The data that support the findings of this study are available from the corresponding author upon reasonable request.

References

[1] Y. Ma, Y.Z. Ma, Z.Q. Zhou, C.F. Li, G.C. Guo, One-hour coherent optical storage in an atomic frequency comb memory, Nat. Commun. 12 (2021) 2381.
[2] T. Zhong, J. Kindem, J. Bartholomew, J. Rochman, I. Craiciu, E. Miyazono, M. Bettinelli, E. Cavalli, V. Verma, S. Nam, et al., Nanophotonic rare-earth quantum memory with optically controlled retrieval, Science 357 (2017) 1392–1395.
[3] B. Lvosky, A. Sanders, W. Titte, Optical quantum memory, Nat. Photonics 3 (12) (2009) 706–714.
[4] C. Clausen, I. Usmani, F. Bussières, N. Sangouard, M. Afzelius, H. de Riedmatten, N. Gisin, Quantum storage of photonic entanglement in a crystal, Nature 469 (2011) 508–511.
[5] M. Xiao, Y.Q. Li, S.Z. Jin, J. Gea-Banacloche, Measurement of dispersive properties of electromagnetically induced transparency in rubidium atoms, Phys. Rev. Lett. 74 (1995) 666.
[6] Y. Zhang, A.W. Brown, M. Xiao, Opening four-wave mixing and six-wave mixing channels via dual electromagnetically induced transparency windows, Phys. Rev. A. 99 (2007) 123603.
[7] H. Wu, Y. Ruan, Z. Li, M.X. Dong, M. Cai, J. Tang, L. Tang, H. Zhang, M. Xiao, K. Xia, Fundamental distinction of electromagnetically induced transparency and autler-townes splitting in breaking the time-reversal symmetry, Laser Photon. Rev. 16 (2022) 2100708.
[8] J. Li, J. Zhu, M. Imran, H. Fan, A. Mujahid, F. Nadeem, P. Li, Y. Zhang, Superior atomic coherence time controlled by crystal phase transition and optical dressing, Opt. Lett. 47 (2022) 2310–2313.
[9] B. Singh, M. Vogl, S. Wurmehl, S. Aswartham, B. Büchner, P. Kumar, Coupling of lattice, spin, and intra-configurational excitations of Eu^{3+} in Eu_2ZnIrO_6, Phys. Rev. Res. 2 (2020) 043179.
[10] R. Mittal, M. Gupta, B. Singh, L. Pintschovius, Y. Zavartsev, S. Chaplot, Phonon dispersion relation, high-pressure phase stability, and thermal expansion in YVO_4, Phys. Rev. Mater. 3 (2019) 043608.
[11] Y. Liu, D. Tu, H. Zhu, X. Chen, Lanthanide-doped luminescent nanoprobes: controlled synthesis, optical spectroscopy, and bioapplications, Chem. Soc. Rev. 42 (2013) 6924–6958.
[12] W. Zheng, P. Huang, D. Tu, E. Ma, H. Zhu, X. Chen, Lanthanide-doped upconversion nano-bioprobes: electronic structures, optical properties, and biodetection, Chem. Soc. Rev. 44 (2015) 1379–1415.
[13] F. Nadeem, M. Usman, A. Mujahid, M. Imran, I. Hussain, U. Javed, M.W. Usmani, M.F. Ather, B. Li, Y. Zhang, Spectral non-hermitian quantization line shape controlled by phonon dressing in various phases of Eu^{3+}: $BiPO_4$, J. Mat. Chem. C. 11 (2023) 11001–11009.
[14] A. Carneiro, O. Malta, Glowing nanocrystals enable 3D X-ray imaging, Nature 590 (2021) 396–397.
[15] P. Li, T. Yuan, F. Li, Y. Zhang, Phosphate ion-driven $BiPO_4$: Eu^{3+} phase transition, J. Phys. Chem. C 123 (7) (2019) 4424–4432.
[16] S.T. Ehsan, A. Tran, F. Blaha, Study of the electronic properties and the cubic to tetragonal phase transition in $RbCaF_3$, Phys. Rev. Mater. 2 (2018) 093610.
[17] H. Fan, F. Raza, I. Ahmed, K. Li, H. Ullah, Y. Zhang, Three-type Fano interference controlled by the phase transition of Eu^{3+}/Pr^{3+}: YPO_4, New J. Phys. 22 (9) (2020) 93008.
[18] I. Hussain, F. Nadeem, M.Q. Khan, M. Usman, H. Fan, P. Li, Y. Zhang, Photon–phonon destructive–constructive polarization quantization in Sm^{3+}: $BiPO_4$, Opt. Lett. 50 (1) (2024) 61–64.
[19] H. Fan, F. Raza, A. Mujahid, Y. Wang, H. Tang, M. Usman, B. Li, C. Li, Y. Zhang, Deterministic relation between thermal-phonon dressings and a Non-Hermitian multi-fano interferences router in ion-doped microcrystals, Chip 3 (1) (2024) 100077.
[20] H. Hodaei, A.U. Hassan, S. Wittek, H. Garcia-Gracia, R. El-Ganainy, D. N. Christodoulides, M. Khajavikhan, Enhanced sensitivity at higher-order exceptional points, Nature 548 (2017) 7666.
[21] M.A. Miri, A. Alu, Exceptional points in optics and photonics, Science 363 (2019) 7709.
[22] S. Baek, S.H. Park, D. Oh, K. Lee, S. Lee, H. Lim, Non-Hermitian chiral degeneracy of gated graphene metasurfaces, Light Sci. Appl. 12 (2023) 87.
[23] A. Opala, M. Furman, M. Król, R. Mirek, K. Tyszka, B. Seredyński, B. Piętka, Natural exceptional points in the excitation spectrum of a light-matter system, Nat. Commun. 10 (2023) 1111.
[24] A. Alivisatos, Semiconductor clusters, nanocrystals, and quantum dots, Science. 271 (1996) 933–937.
[25] P. Li, F. Li, X. Zhang, Y. Li, X. Luo, R. Wang, Y. Cai, Y. Zhang, Orthogonally polarized luminescence of single bismuth phosphate microcrystal doped with europium, Adv. Opt. Mater. 8 (2020) 2000583.
[26] P. Li, Y.X. Guo, A. Liu, X. Yue, T.L. Yuan, J.P. Zhu, Y. Zhang, F. Li, Deterministic relation between optical polarization and lattice symmetry revealed in ion-doped single microcrystals, ACS Nano 16 (2022) 9535–9545.
[27] Z. Nie, H. Zheng, P. Li, Y. Yang, Y. Zhang, M. Xiao, Interacting multi-wave mixing in a five-level atomic system, Phys. Rev. A 77 (6) (2008) 063829.
[28] N.C. Passler, X. Ni, G. Hu, J.R. Matson, G. Carini, M. Wolf, M. Schubert, M, A. Alù, J.D. Caldwell, T.G. Folland, Hyperbolic shear polaritons in low-symmetry crystals, Nature 602 (7898) (2022) 595–600.
[29] B. Romero, S. Bruque, M.A. G Aranda, J.E. Iglesias, Syntheses, crystal structures, and characterization of bismuth phosphates, Inorg. Chem. 33 (9) (1994) 1869–1874.
[30] A.C. Tello, M. Assis, R. Menasce, A.F. Gouveia, V. Teodoro, N. Jacomaci, M. A. Zaghete, Microwave-driven hexagonal-to-monoclinic transition in BiPO4: an in-depth experimental investigation and first-principles study, Inorg. Chem. 59 (11) (2020) 7453–7468.
[31] Z. Hui, B. Xiaofeng, W. Yuanhong, H. Dongdong, G. Jiamin, Li Lu, Li Xiaohui, Y. Shuangyi, Bi2O2Te nanosheets saturable absorber-based passive mode-locked fiber laser: from soliton molecules to harmonic soliton, Adv. Opt. Mater. 10 (24) (2022) 2201812.
[32] Li Xiaohui, X. Huang, X. Hu, X. Guo, Y. Han, Recent progress on mid-infrared pulsed fiber lasers and the applications, Opt. laser tech. 158 (2023) 108898.
[33] Li Xiaohui, W. Xu, Y. Wang, X. Zhang, Z. Hui, H. Zhang, S. Wageh, O.A. Al-Hartomy, A.G. Al-Sehemi, Optical-intensity modulators with PbTe thermoelectric nanopowders for ultrafast photonics, Appl. Math. 28 (2022) 101546.
[34] Z. Chenxi, X. Li, E. Chen, H. Liu, P.P. Shum, X. Chen, Hydrazone organics with third-order nonlinear optical effect for femtosecond pulse generation and control in the L-band, Opt. laser tech. 151 (2022) 108016.
[35] M. Usman, I. Hussain, F. Munir, M.K. Majeed, F. Nadeem, U. Javed, Y. Zhang, Atomic-like Autler–townes splitting controlled by destructive and constructive natural Non-Hermitian quantization in Eu^{3+}: $BiPO_4$, J. Appl. Phys. 135 (24) (2024) 243103.
[36] I. Hussain, U. Javed, F. Munir, M.W. Usmani, F. Nadeem, Mudassir, M. Shehbaz, P. Li, Y. Zhang, Natural Non-Hermitian interaction alignment with photon phonon quantization in Eu^{3+}: $NaYF_4$, Res. in Phys. 62 (2024) 107831.